International Journal of Greenhouse Gas Control 53 (2016) 284–291

Contents lists available at ScienceDirect

International Journal of Greenhouse Gas Control

journal homepage: www.elsevier.com/locate/ijggc

Flow regime analysis for geologic CO_2 sequestration and other subsurface fluid injections

Bo Guo[a,*], Zhong Zheng[b], Karl W. Bandilla[a], Michael A. Celia[a], Howard A. Stone[b]

[a] Department of Civil and Environmental Engineering, Princeton University, United States
[b] Department of Mechanical and Aerospace Engineering, Princeton University, United States

ARTICLE INFO

Article history:
Received 11 April 2016
Received in revised form 15 July 2016
Accepted 9 August 2016
Available online 21 August 2016

Keywords:
Geologic carbon sequestration
CO_2 plume
Sharp interface model
Vertical equilibrium model
Flow regime
Subsurface fluid injection

ABSTRACT

Carbon dioxide (CO_2) injection into a confined saline aquifer may be modeled as an axisymmetric two-phase flow problem. Assuming the CO_2 and brine segregate quickly in the vertical direction due to strong buoyancy, and neglecting capillary pressure and miscibility, the lubrication approximation leads to a one-dimensional nonlinear advection-diffusion equation that describes the evolution of the sharp CO_2-brine interface. The interface evolution is driven by two forces: the force from fluid injection (the lateral pressure gradient due to injection), and buoyancy. Analytical solutions can be derived when one of the two forces is dominant. The solutions depend on the viscosity ratio (M) between the displaced and injected fluids, and a buoyancy parameter (Γ) that measures the relative importance of buoyancy compared to the driving force from injection. Different combinations of these two parameters give different forms of the solutions. But for all the solutions, the radius of the lateral spreading of the injected fluid follows, $r \propto t^{1/2}$ with the proportionality coefficient differing for the different solutions. In this paper, we identify the kinds of solutions appropriate for practical CO_2 injection projects as well as other subsurface fluid injection applications. We use data from eight CO_2 injection projects, twenty-four acid gas injection projects, two liquid waste disposal projects, and one CO_2-WAG enhanced oil recovery project. The solutions provide guidance for the expected behavior of fluid spreading under the different injection operations while providing general insights into overall fluid flow behavior.

1. Introduction

Sequestration of carbon dioxide (CO_2) into deep saline aquifers is considered a promising technology to mitigate anthropogenic CO_2 emissions into the atmosphere (Pacala and Socolow, 2004; IPCC, 2005; Michael et al., 2010; Celia et al., 2015). CO_2 injection into a saline aquifer involves flow of both the injected CO_2 and the resident brine. Understanding such multi-phase flows is important to address questions related to CO_2 injectivity, containment of both CO_2 and brine, and the overall long-term effectiveness of the storage operation.

Injection depths are usually chosen so that the injected CO_2 will be in a supercritical state. While the supercritical CO_2 has density much larger than gaseous CO_2, it is still small relative to the density of the resident brine, with a difference ranging from 250 kg/m^3 to up to 950 kg/m^3, depending on formation depth, geothermal gradient, pressure gradient, surface temperature, and water salinity (Nordbotten and Celia, 2012). Such density differences lead to strong buoyancy that drives CO_2 upward, which in turn leads to vertical segregation between CO_2 and brine in the geologic formation. When the time scale associated with buoyant segregation is small relative to the time scales for horizontal propagation, we can assume that buoyant segregation has occurred, and that CO_2 and brine have reached pressure equilibrium in the vertical direction. This vertical equilibrium assumption has been considered to be reasonable, especially at later times in the injection process (Lyle et al., 2005; Nordbotten and Celia 2006; Nilsen et al., 2011; Court et al., 2012; Pegler et al., 2014; Zheng et al., 2015) as well as the subsequent post-injection time period (Hesse et al., 2008; Gasda et al., 2011; Szulczewski et al., 2012; Zheng et al., 2013). Further assumptions of negligible capillary pressure and negligible miscibility between CO_2 and brine lead to a model where the less-dense injected fluid overrides the displaced (more dense) fluid and the two fluids form a sharp fluid-fluid interface (see Fig. 1). Throughout this paper, we will consider a general set of injected and displaced fluids, not necessarily CO_2 and brine, since the methodology also

* Correspondence to: Bo Guo, now at Department of Energy Resources Engineering, Stanford University, United States.
E-mail addresses: boguo@stanford.edu, guobo07@gmail.com (B. Guo).

http://dx.doi.org/10.1016/j.ijggc.2016.08.007
1750-5836/

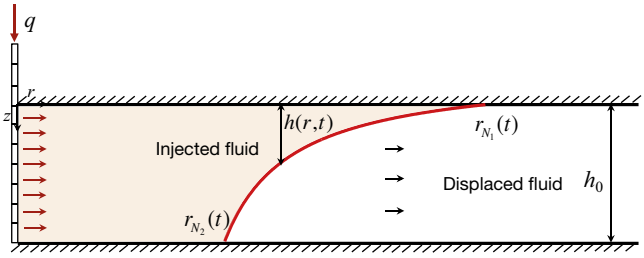

Fig. 1. Schematic of fluid injection into a confined aquifer with the vertical equilibrium and sharp interface assumptions. Here we depict a vertical cross-section of a radial domain, where the origin is located at the center of the injection well and the top of the aquifer (vertical direction is positive downward). The diameter of the injection well is assumed to be negligibly small relative to the typical propagation distance of the injected fluid, and the aquifer is assumed to extend to infinity in the horizontal direction. Here r represents the distance from the center of the injection well and h_0 is the thickness of the aquifer. The shaded area with light orange color indicates the extent of the plume of the injected fluid (CO_2). The injected (CO_2) and displaced (brine) fluids are separated by a sharp interface indicated by the red curve in the figure. Also, $r_{N_1}(t)$ is defined as the leading edge of the plume of the injected fluid and $r_{N_2}(t)$ is defined as the trailing edge. (For interpretation of the references to colour in this figure legend, the reader is referred to the web version of this article.)

applies to other subsurface fluid injection processes such as acid gas injection and liquid waste disposal.

We assume a homogeneous geologic formation with simple geometries, e.g., horizontal and impermeable top and bottom boundaries. For the vertical equilibrium and sharp interface model, we can derive a one-dimensional (1D) nonlinear advection-diffusion equation for the propagation of the CO_2-brine sharp interface. Here, we focus on the injection process through vertical wells, which corresponds to an axisymmetric flow and for which similarity solutions can be found (Lyle et al., 2005; Nordbotten and Celia, 2006; Guo et al., 2016). In the vertical equilibrium model, the vertical flow is negligible as the two fluids are assumed to have already segregated. The horizontal flow is driven by two forces: the force from the fluid injection process (the lateral pressure gradient due to injection), and buoyancy. Analytical solutions can be derived when one of the two forces is dominant. Recently, for this injection scenario and assumptions, Guo et al. (2016) developed a flow regime diagram to identify the range of applicability of the different solutions to this problem. The axes of the diagram are the viscosity ratio (M) between the displaced and the injected fluid and a buoyancy parameter (Γ) that measures the relative importance of buoyancy compared to the force from injection. We note that M is actually the mobility ratio. In this paper, we neglected the residual saturations of the two fluids. Thus, the relative permeabilities of the two fluids are both equal to one under the vertical equilibrium and sharp interface assumptions, and M becomes the viscosity ratio. The diagram has five flow regimes, four of which have analytical solutions (see Fig. 2). Regimes I–III are for injection-dominated (injection-driven) flow, but with the injected fluid being more viscous, equally viscous, and less viscous than the displaced fluid, respectively. Regime IV corresponds to buoyancy-dominated (buoyancy-driven) flow, where the behavior of fluid spreading does not depend on the viscosity ratio. Finally, Regime V is a transition regime, in which the forces from fluid injection and buoyancy are comparable, and where no analytical solution is available. The radius of the lateral fluid spreading follows $r \propto t^{1/2}$ in all flow regimes, while the lateral area of spreading ($\pi r_{N_1}^2(t)$) normalized by that of piston-like spreading is time-independent and is different for each solution (see Fig. 2).

The purpose of this paper is to analyze various injection scenarios and place them in the context of this regime diagram. We use data from eight CO_2 sequestration projects, twenty-four acid gas injection operations, two waste disposal projects, and one CO_2-WAG enhanced oil recovery project. Each of these projects is characterized by the associated dimensionless groups M and Γ, thereby placing each project into one of the flow regimes. For the CO_2 injections, when the project is a pilot-scale study, we also consider how the characterization would change were the injection to be scaled up to an industrial rate.

2. The flow regime diagram

In this section, we briefly review the flow regime diagram from Guo et al. (2016), and highlight some of the flow features in the model of injection and fluid spreading. We consider a horizontal geologic formation with a thickness of h_0 (Fig. 1). The formation is characterized by its porosity and permeability, denoted by ϕ and k respectively; $\Delta\rho = \rho_d - \rho_i$ is the density difference between the displaced (ρ_d) and the injected (ρ_i) fluids and the fluids are assumed incompressible; μ_i and μ_d are viscosities of the injected and the displaced fluids, respectively; and q is the volumetric injection rate. It is natural to use cylindrical coordinates and assume an axisymmetric solution. We consider the vertical equilibrium and sharp interface model, and define $h(r,t)$ as the thickness of the injected fluid as a function of the radial distance (r) from the injection well and time (t). $r_{N_1}(t)$ is defined as the leading edge of the plume of the injected fluid (Fig. 1). For this flow system, we can define two dimensionless groups to characterize the flow behaviors,

$$M \equiv \frac{\mu_d}{\mu_i}, \text{ and } \Gamma \equiv \frac{2\pi\Delta\rho g k h_0^2}{\mu_d q}. \tag{1}$$

By definition, M is the viscosity ratio between the displaced and the injected fluids, and Γ is a buoyancy parameter, which represents the relative importance of buoyancy and the force from fluid injection. We note again that M is actually the mobility ratio, but here we do not consider residual saturations of the two fluids, thereby the relative permeabilities of the two fluids are both equal to one under the vertical equilibrium and sharp interface assumptions, and M becomes the viscosity ratio. We note that we can include the residual saturations by simply scaling M by the relative permeabilities, and the rest of the analysis remains the same. The two dimensionless groups M and Γ serve to organize the injection process as they combine fluid properties, geological parameters, and the injection rate. A brief derivation of the governing equations is provided for the vertical equilibrium and sharp interface model in Appendix A. The various associated model assumptions are addressed in Appendix B.

For the vertical equilibrium and sharp interface model, four analytical solutions can be derived in four distinct asymptotic limits (flow regimes) with respect to M and Γ. We summarize the solutions for the four flow regimes (Regimes I–IV) in Table 1. The solutions are derived with dimensionless variables, which are defined as $H = h/h_0$, $R = r/h_0$, and $T = t/\left(2\pi\phi h_0^3/q\right)$. Regimes I–III are for injection-driven flows ($\Gamma \ll 1$), with the injected fluid being more viscous, equally viscous, and less viscous than the displaced fluid for Regimes I, II, and III, respectively. Regime IV describes buoyancy-driven flow ($\Gamma \gg 1$), where the behavior of fluid spreading does not depend on the viscosity ratio. We note that $\Gamma \ll 1$ and $\Gamma \gg 1$ are used as scaling arguments when we derive the analytical solutions in the asymptotic limits, thus the analytical solutions are not necessarily limited to only $\Gamma \ll 1$ or $\Gamma \gg 1$. To obtain the actual boundaries beyond which the analytical solutions are in valid (with a certain threshold of error), we need to compare the analytical solutions to the full numerical solution of the ordinary differential Eq. (A7) in Appendix A subject to the appropriate boundary conditions. Such comparisons give a (M, Γ) flow regime diagram that organizes the different behaviors of fluid spreading (Guo et al., 2016) (see Fig. 2). The boundaries between the flow regimes are defined as the (M, Γ) values that introduce a 10% difference when

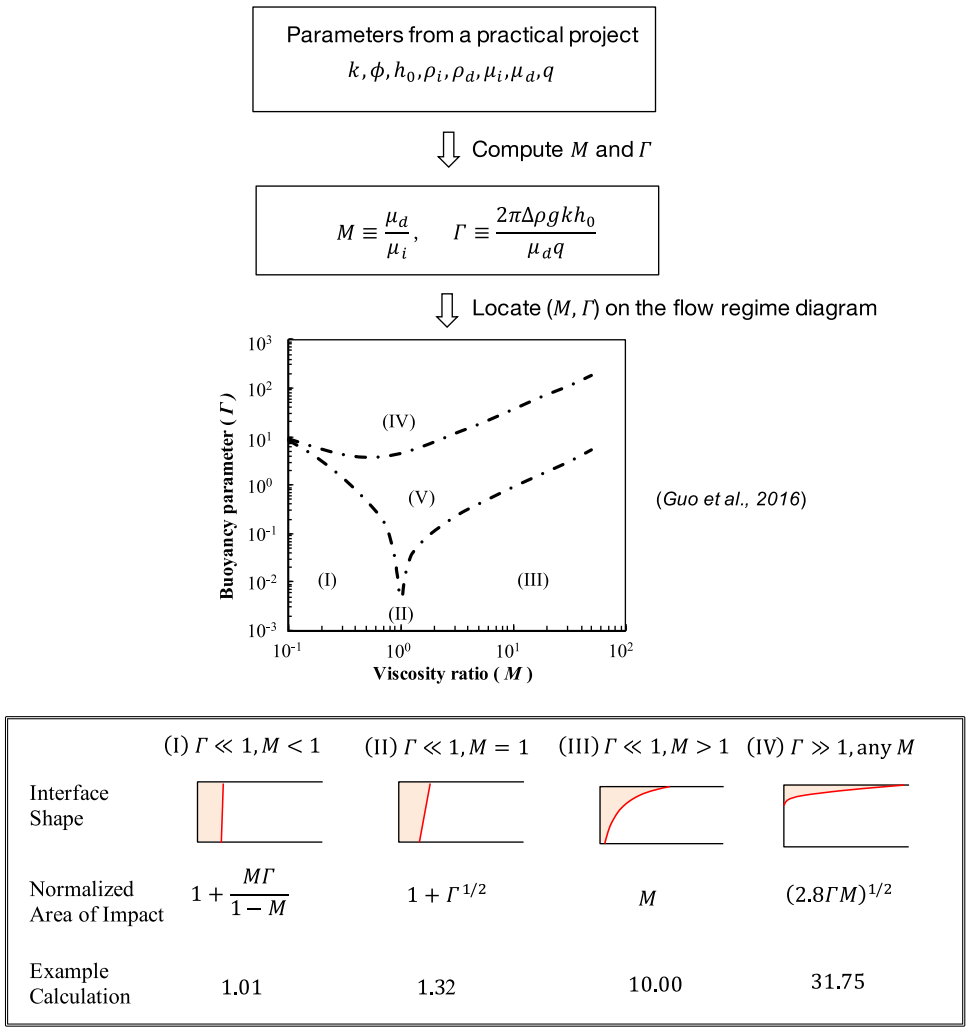

Fig. 2. A flow chart demonstrating the procedure for using the flow regime diagram from Guo et al. (2016) to investigate a practical project. For a specific project, a pair of (M, Γ) values can be computed from the reported parameters. When the pair of (M, Γ) is in Regimes I–IV, the fluid propagation has an analytical solution, otherwise it enters Regime V, where no analytical solution is available. We note that regime II is a line ($M = 1$, $\Gamma \leq 0.7$). The sketches corresponding to each of the flow regimes show the fluid-fluid interface shapes for different analytical solutions. For each case, the time dependence of the spreading of the injected fluid can be evaluated. We also show the expressions of the normalized area of impact, which is time-independent, for all the solutions. An example calculation is shown with the values for M and Γ for the four regimes as: (I)$M = 0.1$, $\Gamma = 0.1$; (II) $M = 1$, $\Gamma = 0.1$; (III) $M = 10$, $\Gamma = 0.1$; (IV) $M = 10$, $\Gamma = 36$.

Table 1
A summary of the analytical solutions for flow Regimes I–IV for nearly horizontal flows in a confined aquifer. The solutions are written in terms of the dimensionless variables (defined in Section 2 and Appendix A). As shown in Fig. 1, we define the intersections between the interface and the top and bottom boundaries of the aquifer as edges of the plume of the injected fluid. The leading edge measures the furthest distance the CO_2 travels from the injection well at any given time. The trailing edge denotes the intersection of the interface with the bottom boundary; there is no trailing edge when the interface does not intersect the bottom boundary. M and Γ are defined in Eq. (1).

Regimes	(M, Γ)	Interface shape	Leading edge	Trailing edge	Reference
I	$M < 1, \Gamma \ll 1$	$H(R,T) = \frac{M-1}{4M\Gamma}\left(R^2/T - 2\right) + 1/2$	$\left(2 + \frac{2M\Gamma}{1-M}\right)^{1/2} T$	$\left(2 - \frac{2M\Gamma}{1-M}\right)^{1/2} T$	Guo et al. (2016)
II	$M = 1, \Gamma \ll 1$	$H(R,T) = \frac{R^2/T-2}{4\sqrt{\Gamma}} + 1/2$	$\left(2 + 2\sqrt{\Gamma}\right)^{1/2} T$	$\left(2 - 2\sqrt{\Gamma}\right)^{1/2} T$	Guo et al. (2016)
III	$M > 1, \Gamma \ll 1$	$H(R,T) = \left(\sqrt{2M/\left(R^2/T\right)} - 1\right)/(M-1)$	$(2M)^{1/2} T$	$\left(\frac{2}{M}\right)^{1/2} T$	Nordbotten and Celia (2006)
IV	any M, $\Gamma \gg 1$	Obtain by numerical integration	$(11.2\Gamma M)^{1/4} T$	No trailing edge	Lyle et al. (2005)

the respective analytical solution is compared to the full numerical solution of Eq. (A7) in Appendix A, with the difference measured using the similarity transformed $\eta_{N1} = R_{N1}^2/T$ location of the leading edge of the CO_2 plume. The location of the leading edge of the CO_2 plume is chosen because it is an important factor for risk assessment of CO_2 injection, especially for leakage risk assessment. Other criteria may be used to measure the discrepancy, such as the difference associated with the approximate shape of the entire fluid-fluid interface, or the difference in the trailing edge. Different criteria may give quantitatively (slightly) different regime boundaries, but they will not qualitatively change the flow regime diagram. See section V of Guo et al. (2016) for the theoretical basis of the regime boundaries.

We can use this regime diagram to study a practical injection project by computing the dimensionless groups M and Γ from Eq. (1). Fig. 2 shows a flow chart that demonstrates a step-by-step procedure for using the flow regime diagram to assess a practical project. Different flow regimes have different engineering implica-

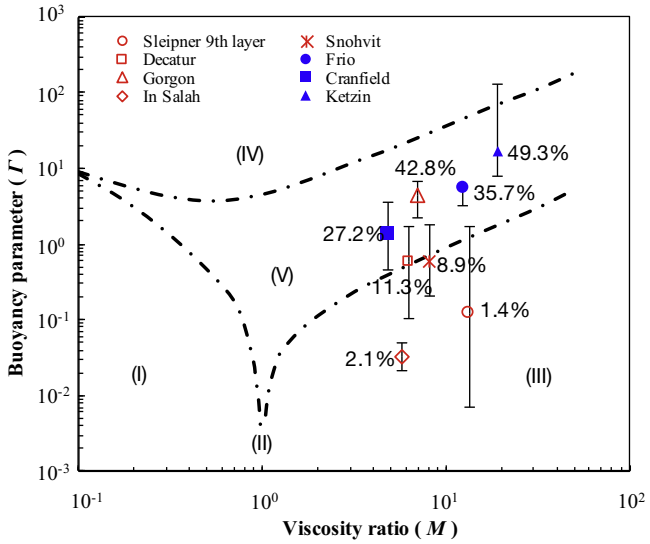

Fig. 3. Flow regime diagram for eight CO_2 injection projects in saline aquifers. The open markers represent projects with industrial-scale injection rates, and the closed markers filled by blue color indicate the projects with pilot-scale injection rates. The five flow Regimes I–V are separated by black dash-dot lines (Guo et al., 2016). The numbers marked besides each point are the differences introduced at the location of the leading edge if the analytical solution of Regime III is used instead of the numerical solution to the corresponding boundary value problem. Detailed data for computing M and Γ can be found in Table 2 and in Appendix B.

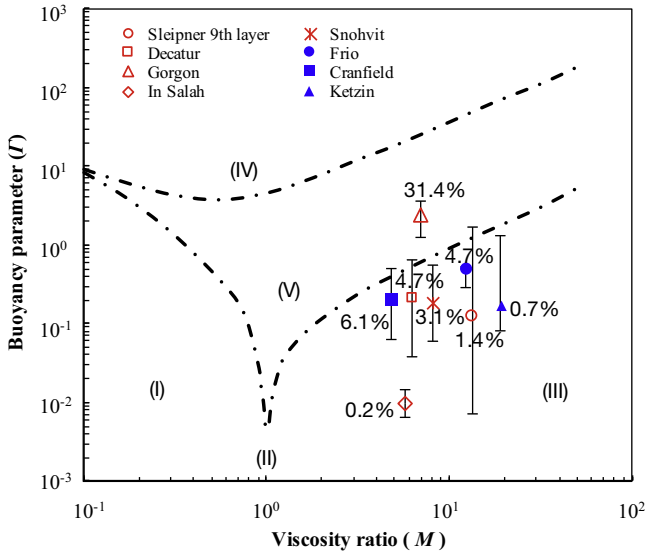

Fig. 4. Flow regimes for the eight CO_2 injection projects into saline aquifers with a (hypothetical) industrial-scale injection rate of 1 Mt/year.

tions, e.g., different regimes have different areas of spreading for a given amount of injected fluid. To understand the area of spreading we introduce the concept of normalized area of impact, which is defined as the lateral radial area occupied by a given volume of injected fluid normalized by the lateral radial area from a piston-like displacement (where the fluid-fluid interface is vertical). The greater the normalized area, the further a given amount of the injected fluid spreads. The analytical expressions for the normalized area of impact for each of the regimes are presented in Fig. 2, where we also show an example calculation to give a sense of the values of the normalized areas of impact, which are independent of time. The results show that the buoyancy-driven regime has a much larger area of impact compared to the injection-driven regimes for a fixed volume of injected fluid, and for the injection-driven solutions, higher viscosity ratios lead to more spreading. The transition regime would have an area of impact in between the injection-driven and buoyancy-driven flow regimes. The information from the normalized area of impact can be used to assess the risks associated with fluid spreading for practical injection projects, especially in the early stage of the project when not much data are available.

3. Flow regime analysis

In this section, we use the flow regime diagram to study various kinds of injection operations. Detailed data for different projects are given in Tables 2 and 3, . Further information about the data and the calculations is provided in Appendix C.

3.1. Geologic CO_2 sequestration

The values of dimensionless groups (M, Γ) for eight CO_2 injection projects are shown in Fig. 3 with an associated range of variations in Γ. The percentages indicate the difference between the analytical solution of Regime III and the full solution. The range of Γ values is based on identified ranges of parameters, with most of the variation being associated with values of the permeability. Variations in M are small, and are therefore not shown. Detailed data and estimates of the variations are given in Table 2 and Appendix D. Since the injected CO_2 is always less viscous than the resident brine in the aquifers ($M > 1$), all the projects fall on the right side of the regime diagram (Fig. 3). The injection-driven regime (Regime III) has three projects, corresponding to the Sleipner 9th layer, In Salah, and Snøhvit. The transition regime (Regime V) includes the other five projects: Ketzin, Frio, Cranfield, Decatur, and Gorgon.

The three projects in the injection-driven regime (Regime III) all have relatively large injection rates, with a single-well injection rate of CO_2 larger than 0.3 Mt/year. We note that a larger injection rate leads to a smaller Γ, see Eq. (1). Physically this means that the flow is mainly driven by fluid injection instead of buoyancy. The total injection rate in In Salah was reported to be about 1.28 Mt/year (Michael et al., 2010), and CO_2 was injected through three horizontal wells. We only consider the injection well KB-501, which has an average injection rate of around 0.3 Mt/year. Since we only look at the long-term behavior of the CO_2 plume, we treat the injection well as a point source equivalent to a vertical well. For the Sleipner project, we only consider CO_2 migration in the upper-most (the 9th) layer and treat the input source of CO_2 from below as a continuous injection. For the Snøhvit project, it has been shown that CO_2 was contained in Tubåen 1 by the overlying shale unit (Grude et al., 2014); thus, we only consider the Tubåen 1 sandstone unit in the lower part of the Tubåen formation.

The three pilot projects (Keztin, Frio, and Cranfield) and the Gorgon and Decatur projects are all in the transition regime (Regime V). Among the three pilot projects, Cranfield has the largest injection rate (0.14 Mt/year). The Gorgon project has an injection rate of 0.56 Mt/year for a single well, but it is still in the transition regime due to its reported large thickness $h_0 = 250$m, which leads to a large value of Γ. The Decatur project is near the boundary of Regimes III and V, being slightly in Regime V.

We next consider scenarios where all the projects are scaled up to an industrial scale, with injection rates increased to 1 Mt/year, because any actual practical project would necessarily inject large amounts of CO_2 (IPCC 2005; Meng et al., 2007; Michael et al., 2010; Zheng et al., 2010). With the increased injection rate, all of the (M, Γ) pairs for the pilot projects shift down to the injection regime as shown in Fig. 4, with only the Gorgon project remaining in Regime V due to its very large formation thickness. These calculations suggest that the analytical solution of Regime III is the appropriate choice for the sharp-interface model involving large-scale CO_2 injection.

Table 2
Data and parameters for CO_2 sequestration projects in saline aquifers. h_0 is the thickness of the aquifer, ϕ is porosity, k is permeability, q is the mass injection rate for a single well, and M and Γ are the dimensionless groups defined in Eq. (1).

Project	Scale	h_0 (m)	ϕ (−)	k (mD)	q (Mt/y)	M (−)	Γ (−)	Difference (%)
Ketzin	Pilot	73	0.23	100	0.01	19.08	16.90	49.3
Cranfield	Pilot	24	0.30	270	0.14	5.23	1.42	27.2
Frio	Pilot	24	0.30	1400	0.09	12.34	5.45	35.7
Decatur	Demonstration	46	0.15	120	0.37	6.28	0.58	11.3
Sleipner	Commercial	11.3	0.36	2000	1	13.33	0.12	1.4
Snohvit	Commercial	14	0.19	750	0.3	8.07	0.60	8.9
In Salah	Commercial	20	0.17	20	0.3	5.77	0.03	2.1
Gorgon	Commercial	250	0.20	25	0.56	7.02	4.36	42.8

Table 3
Parameters and data for CO_2-WAG EOR and waste disposal projects. ρ_d and ρ_i are density of the displaced fluid and the injected fluid, respectively; μ_d and μ_i are the viscosity of the displaced fluid and the injection fluid, respectively. Other variables have the same definitions as those in Table 2.

Project	h_0 (m)	ϕ (−)	k (mD)	ρ_d (kg/m^3)	μ_d (mPa s)	ρ_i (kg/m^3)	μ_i (mPa s)	q (m^3/s)	M (−)	Γ (−)
Waste disposal 1	15.2	0.07	69	1094	0.893	1006	0.668	0.0063	1.34	0.02
Waste disposal 2	50	0.32	695	1085	0.686	1195	1.220	0.0033	0.56	5.28
EOR (water to CO_2)	81	0.04	19.4	670	0.062	994	0.445	0.16	0.14	0.26
EOR (CO_2 to water)	81	0.04	19.4	994	0.445	670	0.062	0.16	7.18	0.04

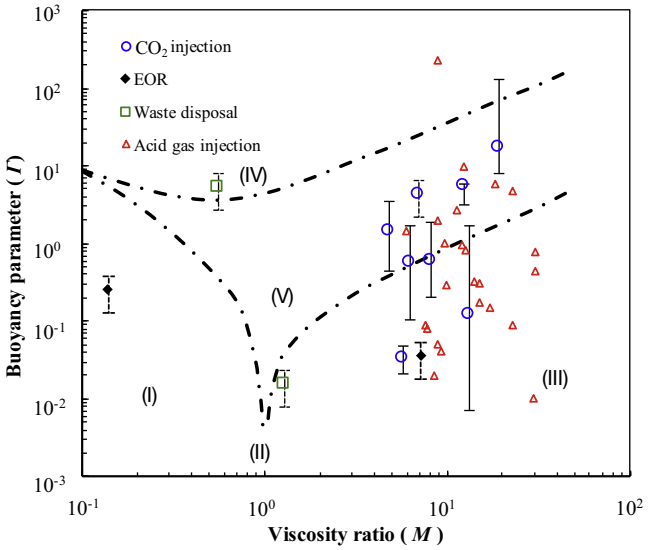

Fig. 5. Flow regime diagram for eight CO_2 injection projects, twenty-four acid gas injection projects, two waste disposal projects, and one CO_2-WAG EOR project.

3.2. Other subsurface fluid injection projects

We have also computed the dimensionless pairs (M, Γ) for twenty-four acid gas injection projects, based on data from Bachu et al. (2005), and placed them onto the flow regime diagram (see Fig. 5). The majority of the projects (sixteen out of twenty-four) lie in the injection-driven regime (Regime III), one project lies in the buoyancy-driven regime (Regime IV), and seven projects lie in the transition regime (Regime V). We note that Γ is small for many of the acid gas projects although the injection rates are not large, which is mainly because the formations are reported to be thin and have low permeability. Detailed data for the acid gas injection projects is provided in Appendix D. We note that Bachu et al. (2005) analyzed the same dataset for the acid gas injection projects, where they used empirically assigned regime boundaries for Regime III ($\Gamma = 0.5$) and Regime IV ($\Gamma = 10$), with no dependence on M. Here we base our analysis on a systematically developed flow regime diagram.

In addition, we consider a CO_2-WAG EOR project and two subsurface waste disposal projects. For the CO_2-WAG EOR project, we focus on the fluid-fluid interface between water and CO_2, which includes (more viscous) water pushing (less viscous) CO_2, as well as CO_2 displacing water. Based on the parameters from Kane (1979), these two displacement cases fall in Regimes I and III. The two waste disposal projects include liquid waste injection into a carbonate aquifer and a sandstone aquifer, respectively. Depending on the salinity of the injected and displaced fluids, for a waste disposal project, the injected fluid can be either more viscous or less viscous than the displaced fluid. Here we use the parameters from Ortoleva and Liu (1995) and consider two scenarios. One corresponds to the buoyancy-driven regime (Regime IV) and the other lies in the injection-driven regime (Regime III), as shown in Fig. 5. An estimated variation of ±50% in permeability is given to each of the projects for CO2-WAG EOR and subsurface waste disposal, which yields a ±50% variation in the Γ values.

4. Conclusions

In this paper, we collected data from various injection projects that involve fluid injection into deep formations and investigated the behaviors of fluid spreading for each of the projects, using the flow regime diagram from Guo et al. (2016). Among the eight geologic CO_2 sequestration projects we considered, including both industrial-scale and pilot-scale projects, three (all industrial-scale) fall within in the injection-driven regime (Regime III), while the other five (mostly pilot-scale) are in the transition regime (Regime V). We note that although the regime of a project depends on various parameters that contribute to the dimensionless groups (M, Γ), the injection rate is a significant controlling parameter. If an industrial-scale injection rate of 1 Mt/year is applied to the pilot-scale projects, all of the pilot-scale projects move into the injection-driven regime (Regime III). In addition to CO_2 injection, we showed that almost all of the acid-gas injection operations fall within Regime III or V, while CO_2-WAG EOR and liquid waste disposal injections can populate Regimes I, II, and IV. This flow regime analysis provides insights into the flow processes and serves to guide the choice of simplified models and analytical solutions that can be applied to different kinds of injection scenarios. Finally, we have noted that the normalized area of spreading is time independent and only depends on the associated values of M and Γ.

Acknowledgements

This work was supported in part by the Department of Energy under Grant No. DE-FE0009563 and the Princeton Carbon Mitigation Initiative (CMI). We thank I. C. Christov, J. M. Nordbotten and R.H. Socolow for helpful discussions. Z. Zheng also thanks the Princeton Environmental Institute for partial support through the CMI Young Investigator Award.

Appendix A. The model

In this section, we give a brief summary of the vertical equilibrium and sharp interface model from Guo et al. (2016). As shown in Fig. 1, we consider a horizontal geologic formation with a thickness h_0; ϕ and k are the porosity and permeability of the geologic formation, respectively; $\Delta\rho = \rho_d - \rho_i$ is the density difference between the displaced (ρ_d) and the injected (ρ_i) fluids; μ_i and μ_d are viscosities of the injected and the displaced fluids, respectively; and q is the volumetric injection rate. It is natural to use cylindrical coordinates and assume an axisymmetric solution, and we define $h(r,t)$ as the (saturated) thickness of the injected fluid as a function of the radial distance (r) from the injection well and time (t). $r_{N_1}(t)$ is defined as the leading edge of the plume of the injected fluid.

By combining the mass balance equations and the volumetric flux equation (Darcy's equation), we obtain a one-dimensional-in-space nonlinear advection-diffusion equation for the propagation of the fluid-fluid interface $h(r,t)$

$$\frac{\partial h}{\partial t} - \frac{1}{\phi r}\frac{\partial}{\partial r}\left(\frac{\Delta\rho g k h(h_0-h)r}{\mu_d h + \mu_i(h_0-h)}\frac{\partial h}{\partial r} + \frac{q\mu_i(h_0-h)}{2\pi(\mu_d h + \mu_i(h_0-h))}\right) = 0. \tag{A1}$$

We consider a geologic formation whose pore space is originally filled with the displaced fluid, thus the initial condition is

$$h(r,0) = 0. \tag{A2}$$

Two boundary conditions are needed. One is at the leading edge ($r_{N_1}(t)$) of the plume of the injected fluid, where the height of the injected fluid is zero; the other is at the origin (the location of the injection well), where the volumetric injection rate is q. The conditions are

$$h\left(r_{N_1}(t), t\right) = 0, \tag{A3}$$

$$\left[\frac{\Delta\rho g k h(h_0-h)r}{\mu_d h + \mu_i(h_0-h)}\frac{\partial h}{\partial r} + \frac{q\mu_i(h_0-h)}{2\pi(\mu_d h + \mu_i(h_0-h))}\right]\Big|_{r=0} = \frac{q}{2\pi}, \tag{A4}$$

where Eq. (A4) is obtained by integrating Eq. (A1) with respect to r from the origin to the leading edge of the plume.

A non-dimensional version of Eq. (A1) can be obtained by defining $H = h/h_0$, $R = r/h_0$, $T = t/\left(\frac{2\pi\phi h_0^3}{q}\right)$, and using these to transform to an equation for $H(R,T)$:

$$\frac{\partial H}{\partial T} - \frac{1}{R}\frac{\partial}{\partial R}\left(\frac{\Gamma M H(1-H)R}{1+(M-1)H}\frac{\partial H}{\partial R} + \frac{1-H}{1+(M-1)H}\right) = 0, \tag{A5}$$

where we define two dimensionless groups

$$M \equiv \frac{\mu_d}{\mu_i}, \text{ and } \Gamma \equiv \frac{2\pi\Delta\rho g k h_0^2}{\mu_d q}. \tag{A6}$$

By definition, M is the viscosity ratio between the displaced fluid and the injected fluid, and Γ is a buoyancy parameter, which represents the relative importance of buoyancy and the force from fluid injection. We note that M is actually the mobility ratio. As was pointed out in the main text of the paper, we have neglected the residual saturations of two fluids. Thus the relative permeabilities are both equal to one under the vertical equilibrium and sharp interface assumptions, and $M = \frac{\mu_d}{\mu_i}$.

The dimensionless form of the initial and boundary conditions can also be derived. Then, with the definition of the similarity variable $\eta = R^2/T$, Eq. (A5) becomes an ordinary differential equation

$$\eta\frac{dH}{d\eta} + 2\frac{d}{d\eta}\left(\frac{2\Gamma M H(1-H)\eta}{1+(M-1)H}\frac{dH}{d\eta} + \frac{1-H}{1+(M-1)H}\right) = 0. \tag{A7}$$

The two boundary conditions with respect to the new variable η can also be derived (given by Guo et al. (2016)). Eq. (A7), in general, does not have analytical solutions, but it can be solved analytically in the four asymptotic limits. The four analytical solutions are summarized in Table 1, which correspond to Regimes I, II, III, and IV. We note that the form of the similarity variable implies that the location of the leading edge $R_{N_1} \propto T^{1/2}$. Thus, relative to a uniform injection front, i.e. piston-like injection, which also would advance proportional to $T^{1/2}$, the ratio of the lateral area of spreading for a given volume of injected fluid between the analytical solutions and piston-like injection is independent of time.

Appendix B. Model assumptions

In this section, we discuss the assumptions and limitations for the vertical equilibrium and sharp interface model. The entire analysis of this paper relies on the vertical equilibrium and sharp interface assumptions. The validity of the vertical equilibrium assumption depends on the time scale associated with the vertical buoyant segregation and the aspect ratio (length to thickness) of the aquifer. Lake (1989) and Yortsos (1995) discussed the appropriateness of the vertical equilibrium assumption with respect to the aspect ratio of the geometry of the geologic formation and the difference between the permeabilities in the horizontal and vertical directions. Nordbotten and Dahle (2011) analyzed the impact of the capillary transition zone on the vertical equilibrium models and Court et al. (2012) investigated the validity of the vertical equilibrium and sharp interface assumptions in practical simulations for CO_2 storage. The vertical equilibrium assumption has been generally considered reasonable for homogeneous geologic formations with relatively high permeability. This is especially true for later times during the injection period and the subsequent post-injection time period. For geologic formations with low permeability and heterogeneities, the time scale for the assumption to be valid may be longer, and other solution strategies need to be applied (Guo et al., 2014).

Here, we estimate the time scale of vertical segregation and the travel distance of the injected fluid plume for which the vertical equilibrium assumption is applicable. The time scale for the two fluids to segregate (t_s) in the vertical direction can be estimated as (Nordbotten and Dahle, 2011)

$$t_s \approx \frac{h_0\phi}{\Delta\rho g k_z \lambda_d^*} \tag{A8}$$

where k_z is the vertical permeability of the geologic formation, and $\lambda_d^* = k_{r,d}^*/\mu_d$ indicates the characteristic mobility of the displaced fluid, with $k_{r,d}^*$ being the characteristic relative permeability for the displaced fluid. For the vertical equilibrium assumption to be valid, the time of horizontal spreading (t) needs to be larger than the segregation time scale (t_s), i.e.

$$t \geq t_s \tag{A9}$$

Now, we estimate the horizontal distance the injected fluid travels for time t. Here, we consider an example of a less viscous fluid displacing a more viscous fluid in both the buoyancy-driven and the injection-driven cases.

For the buoyancy-driven regime, the leading edge of the injected fluid follows

$$\frac{R_{N_1}^2}{T} = \left(\frac{2\Gamma M}{0.18}\right)^{1/2} \tag{A10}$$

Thus,

$$t = T\frac{2\pi\phi h_0^3}{q} = R_{N_1}^2\left(\frac{0.18}{2\Gamma M}\right)^{\frac{1}{2}}\frac{2\pi\phi h_0^3}{q} \tag{A11}$$

Substituting $t \geq t_s$ to Eqs. (A8) and (A11), we obtain

$$R_{N_1} \geq \left(\frac{k_x}{k_z}\right)^{\frac{1}{2}}\left(\frac{M}{\Gamma}\right)^{\frac{1}{4}}\left(\frac{1}{k_{r,d}^*}\right)^{\frac{1}{2}}\left(\frac{2}{0.18}\right)^{\frac{1}{4}} \tag{A12}$$

We choose a typical value of $(M, \Gamma) = (8, 32)$ in the buoyancy-driven regime, the representative relative permeability $k_{r,d}^* = 1$, and use a horizontal-to-vertical anisotropy ratio of permeabilities$k_x/k_z = 10$. Then, we get $R_{N_1} \geq 4$, which suggests that the horizontal distance of the injected fluid $r_{N_1} = R_{N_1}h_0$ needs to be larger than 4 times the thickness of the geologic formation, that is $r_{N_1} \geq 4h_0$, for the vertical equilibrium assumption to be valid in the buoyancy-driven regime. We note that this estimate depends on $k_{r,d}^*$, which can vary between 0 and 1. For example, $R_{N_1} \geq 13$ for $k_{r,d}^* = 0.1$.

For the injection-driven regime, the leading edge of the injected fluid follows

$$\frac{R_{N_1}^2}{T} = 2M \tag{A13}$$

Similarly, we can obtain

$$R_{N_1} \geq \left(\frac{k_x}{k_z}\right)^{\frac{1}{2}}\left(\frac{2M}{\Gamma}\right)^{\frac{1}{2}}\left(\frac{1}{k_{r,d}^*}\right)^{\frac{1}{2}} \tag{A14}$$

A typical value of $(M, \Gamma) = (8, 0.1)$, $k_{r,d}^* = 1$, and $k_x/k_z = 10$ provide $R_{N_1} \geq 40$. Thus, the horizontal distance of the injected fluid needs to be larger than 40 times the thickness of the geologic formation. We note that $R_{N_1} \geq 125$ for $k_{r,d}^* = 0.1$. We also note that we can estimate the range of time scales for segregation based on the estimates of the travel distance of the injected fluid. For the injection-driven regime, the time scale of segregation $t_s = \frac{R_{N_1}^2}{2M}t_c = \frac{R_{N_1}^2}{2M}\frac{2\pi\phi h_0^3}{q}$. For $(M, \Gamma) = (8, 0.1)$, in the context of CO_2 sequestration, if one considers a formation with a thickness of 25 m, a porosity of 0.15, CO_2 density of 700 kg/m^3, and an injection rate of 1.0 Mt/year, t_s can be computed as from 1 year to 10 years for R_{N_1} ranging from 40 to 125.

When the driving forces from buoyancy and fluid injection are comparable, the horizontal traveling distance is expected to be in between of the estimates for the buoyancy-driven and the injection-driven flow regimes.

Appendix C. Parameter/Data for CO_2 sequestration*

*ρ_b and ρ_c are brine and CO_2 densities respectively, μ_b and μ_c are brine and CO_2 viscosities respectively. For each project, we collect parameters from the literature and compute a reference, an upper bound and lower bound for the buoyancy parameter Γ. The variation of the permeability for the Gorgon project is not reported; here we estimate it as ± 50%, which gives a variation of ± 50% in the value of Γ. The "–" signs in the data entries indicate that the values are the same as the reference values. The sources of the data are listed in the last column.

Project		h_0	ϕ	k	ρ_b	μ_b	ρ_c	μ_c	q	q	M	Γ	Literature
		(m)	(–)	(mD)	(kg/m^3)	(mPa s)	(kg/m^3)	(mPa s)	(Mt/y)	(m^3/s)	(–)	(–)	
Ketzin	Reference	73	0.23	100	1000	1.15	350	0.060	0.01	0.0011	19.08	16.90	Michael et al. (2010),
	Upper	74	–	750	–	–	–	–	–	–	–	130.24	Norden and Frykman (2013)
	Lower	71	–	50	–	–	–	–	–	–	–	7.99	and Streibel et al. (2014)
Cranfield	Reference	24	0.30	270	982.5	0.31	686	0.058	0.14	0.0066	5.23	1.42	
	Upper	–	0.35	400	965	0.23	591	0.048	–	–	4.82	3.52	Doughty and Freifeld (2013)
	Lower	–	0.25	144	1090	0.38	781	0.069	–	–	5.52	0.45	
Frio	Reference	24	0.30	1400	1070	0.63	830	0.051	0.09	0.0035	12.34	5.45	Doughty et al. (2008) and
	Upper	24	–	1500	–	–	–	–	–	–	–	5.84	Michael et al. (2010)
	Lower	19	–	1280	–	–	–	–	–	–	–	3.13	
Decatur	Reference	46	0.15	120	1100	0.50	847	0.080	0.37	0.0137	6.28	0.58	Zhou et al. (2010) , Frailey
	Upper	64	–	185	–	–	–	–	–	–	–	1.73	et al. (2011) and Senel et al.
	Lower	30	–	50	–	–	–	–	–	–	–	0.10	(2014)
Sleipner	Reference	11.3	0.36	2000	1020	0.80	760	0.060	1	0.0417	13.33	0.12	
	Upper	26.3	0.40	5000	–	0.88	529	–	–	–	14.58	1.68	Singh et al. (2013)
	Lower	3.5	0.27	1100	–	0.79	529	–	–	–	13.17	0.01	
Snøhvit	Reference	14	0.19	750	1090	0.44	663	0.055	0.3	0.0145	8.07	0.60	Shi et al. (2013) and
	Upper	15	0.19	2000	–	–	–	–	–	–	–	1.83	Grude et al. (2014)
	Lower	10	0.13	500	–	–	–	–	–	–	–	0.20	
In Salah	Reference	20	0.17	20	978	0.32	678	0.056	0.3	0.0141	5.77	0.03	Iding and Ringrose (2010)
	Upper	–	–	30	–	–	–	–	–	–	–	0.05	and Rutqvist et al. (2010)
	Lower	–	–	13	–	–	–	–	–	–	–	0.02	
Gorgon	Reference	250	0.20	25	968	0.29	529	0.041	0.56	0.0336	7.02	4.36	
	Upper	–	–	37.5	–	–	–	–	–	–	–	6.54	Michael et al. (2010)
	Lower	–	–	12.5	–	–	–	–	–	–	–	2.18	

Appendix D. Parameter/Data for acid gas injection*

Site	H (m)	ϕ (−)	k (mD)	ρ_b (kg/m^3)	μ_b (mPa s)	ρ_c (kg/m^3)	μ_c (mPa s)	q (m^3/s)	M (−)	Γ (−)
1	15	0.06	30	1083.6	0.600	527.5	0.040	2.30E-03	15.00	0.17
2	10	0.18	186	1116.9	0.660	625.7	0.058	3.15E-04	11.38	2.71
3	18	0.05	40	1175.3	0.775	633.7	0.062	6.66E-04	12.50	0.84
4	8	0.1	100	1086.3	0.651	241.4	0.021	1.15E-03	31.00	0.45
5	10	0.07	16	1175.4	0.640	478.6	0.037	7.02E-04	17.30	0.15
6	13	0.12	30	1111.5	0.500	570.3	0.051	1.18E-03	9.80	0.29
7	4	0.13	6	1089.5	0.740	325.4	0.025	4.49E-04	29.60	0.01
8	81	0.04	9	1093.1	0.670	620	0.054	2.59E-04	12.41	9.92
9	29	0.2	6	1113.8	0.630	583	0.052	2.69E-04	12.12	0.97
10	9	0.12	9	1006.8	0.460	561	0.050	1.11E-03	9.20	0.04
11	60	0.09	137	1064.7	0.360	498.2	0.040	2.08E-04	9.00	229.88
12	10	0.06	75	1089.8	0.393	630.9	0.066	3.70E-04	5.95	1.46
13	10	0.08	115	1055.1	0.483	639.8	0.055	3.11E-04	8.78	1.96
14	10	0.12	9	1047.6	0.440	632.9	0.057	5.69E-04	7.72	0.09
15	10	0.06	14	1273	1.320	680.9	0.058	4.53E-04	22.76	0.09
16	40	0.22	67	1060.6	0.820	489	0.036	9.81E-04	22.78	4.69
17	4	0.1	346	1051.9	0.600	204.8	0.020	6.09E-04	30.00	0.79
18	24	0.11	10	1117.5	0.610	639.6	0.064	2.81E-04	9.53	0.99
19	13	0.12	13	1129.5	0.650	653.3	0.073	2.20E-03	8.90	0.05
20	13	0.12	32	1077.7	0.571	653.3	0.073	3.19E-03	7.82	0.08
21	40	0.05	27	1160.7	0.630	446.7	0.034	5.29E-04	18.53	5.71
22	5	0.06	109	1084.5	0.550	500.4	0.039	5.49E-04	14.10	0.33
23	26	0.12	1	1106.5	0.480	571.6	0.056	1.90E-03	8.57	0.02
24	10	0.1	130	1112.8	0.516	449.8	0.035	3.39E-03	14.74	0.30

*This table of data is from Bachu et al. (2005), with corrections made according to the authors (personal communication).

References

Bachu, S., Nordbotten, J.M., Celia, M.A., 2005. Evaluation of the spread of acid gas plumes injected in deep saline aquifers in western Canada as an analogue for CO_2 injection in continental sedimentary basins. In: Rubin, E.S., Keith, D.W., Gilboy, C.F. (Eds.), Proceedings of 7th International Conference on Greenhouse Gas Control Technologies. Elsevier, IEA Greenhouse Gas Programme, Cheltenham, U. K.

Celia, M.A., Bachu, S., Nordbotten, J.M., Bandilla, K.W., 2015. Status of CO_2 storage in deep saline aquifers with emphasis on modeling approaches and practical simulations. Water Resour. Res. 51 (9), 6846–6892.

Court, B., Bandilla, K.W., Celia, M.A., Janzen, A., Dobossy, M., Nordbotten, J.M., 2012. Applicability of vertical-equilibrium and sharp-interface assumptions in CO_2 sequestration modeling. Int. J. Greenh. Gas Control 10, 134–147.

Doughty, C., Freifeld, B.M., 2013. Modeling CO_2 injection at Cranfield Mississippi: investigation of methane and temperature effects. Greenh. Gases Sci. Technol. 3 (6), 475–490.

Doughty, C., Freifeld, B.M., Trautz, R.C., 2008. Site characterization for CO_2 geologic storage and vice versa: the Frio brine pilot Texas, USA as a case study. Environ. Geol. 54 (8), 1635–1656.

Frailey, S.M., Damico, J., Leetaru, H.E., 2011. Reservoir characterization of the Mt. Simon Sandstone, Illinois Basin, USA. Energy Procedia 4, 5487–5494.

Gasda, S.E., Nordbotten, J.M., Celia, M.A., 2011. Vertically averaged approaches for CO_2 migration with solubility trapping. Water Resour. Res. 47, W05528.

Grude, S., Landrø, M., White, J.C., Torsæter, O., 2014. CO_2 saturation and thickness predictions in the Tubåen Fm., Snøhvit field, from analytical solution and time-lapse seismic data. Int. J. Greenh. Gas Control 29, 248–255.

Guo, B., Bandilla, K.W., Doster, F., Keilegavlen, E., Celia, M.A., 2014. A vertically integrated model with vertical dynamics for CO_2 storage. Water Resour. Res. 50 (8), 6269–6284.

Guo, B., Zheng, Z., Celia, M.A., Stone, H.A., 2016. Axisymmetric flows from fluid injection into a confined porous medium. Phys. Fluids 28, 022107.

Hesse, M.A., Orr, F.M., Tchelepi, H.A., 2008. Gravity currents with residual trapping. J. Fluid Mech. 611, 35–60.

IPCC, 2016. IPCC special report on carbon dioxide capture and storage. In: Metz, B., Davidson, O., de Coninck, H., Loos, M., Meyer, L. (Eds.), Prepared by Working Group III of the Intergovernmental Panel on Climate Change. Cambridge Univ. Press, Cambridge, U. K.

Iding, M., Ringrose, P., 2010. Evaluating the impact of fractures on the performance of the In Salah CO_2 storage site. Int. J. Greenh. Gas Control 4 (2), 242–248.

Kane, A.V., 1979. Performance review of a large-Scale CO_2-WAG enhanced recovery project SACROC Unit Kelly-Snyder field. J. Pet. Technol. 31 (02), 217–231.

Lake, L.W., 1989. Enhanced Oil Recovery. Prentice Hall.

Lyle, S., Huppert, H.E., Hallworth, M., Bickle, M., Chadwick, A., 2005. Axisymmetric gravity currents in a porous medium. J. Fluid Mech. 543, 293–302.

Meng, K.C., Williams, R.H., Celia, M.A., 2007. Opportunities for low-cost CO_2 storage demonstration projects in China. Energy Policy, 2368–2378.

Michael, K., Golab, A., Shulakova, V., Ennis-King, J., Allinson, G., Sharma, S., Aiken, T., 2010. Geological storage of CO_2 in saline aquifers—a review of the experience from existing storage operations. Int. J. Greenh. Gas Control 4 (4), 659–667.

Nilsen, H.M., Herrera, P.A., Ashraf, M., Ligaarden, I., Iding, M., Hermanrud, C., Lie, K.A., Nordbotten, J.M., Dahle, H.K., Keilegavlen, E., 2011. Field-case simulation of CO_2-plume migration using vertical-equilibrium models. Energy Procedia 4, 3801–3808.

Nordbotten, J.M., Celia, M.A., 2006. Similarity solutions for fluid injection into confined aquifers. J. Fluid Mech. 561, 307–327.

Nordbotten, J.M., Celia, M.A., 2012. Geological Storage of CO_2: Modeling Approaches for Large-scale Simulation. John Wiley & Sons, Incorporated, Hoboken, New Jersey.

Nordbotten, J.M., Dahle, H.K., 2011. Impact of the capillary fringe in vertically integrated models for CO_2 storage. Water Resour. Res. 47, W02537.

Norden, B., Frykman, P., 2013. Geological modelling of the Triassic Stuttgart formation at the Ketzin CO_2 storage site, Germany. Int. J. Greenh. Gas Control 19, 756–774.

Ortoleva, P., Liu, X., 1995. Coupled reaction-transport modeling of deep well waste injection. In: EPA Report.

Pacala, S., Socolow, R., 2004. Stabilization wedges: solving the climate problem for the next 50 years with current technologies. Science 305 (5686), 968–972.

Pegler, S.S., Huppert, H.E., Neufeld, J. a, 2014. Fluid injection into a confined porous layer. J. Fluid Mech. 745, 592–620.

Rutqvist, J., Vasco, D.W., Myer, L., 2010. Coupled reservoir-geomechanical analysis of CO_2 injection and ground deformations at In Salah Algeria. Int. J. Greenh. Gas Control 4 (2), 225–230.

Senel, O., Will, R., Butsch, R.J., 2014. Integrated reservoir modeling at the Illinois Basin–Decatur Project. Greenh. Gases: Sci. Technol. 4 (5), 662–684.

Shi, J.Q., Imrie, C., Sinayuc, C., Durucan, S., Korre, A., Eiken, O., 2013. Snøhvit CO_2 storage project: assessment of CO_2 injection performance through history matching of the injection well pessure over a 32-months period. Energy Procedia 37, 3267–3274.

Singh, V.P., Cavanagh, A., Hansen, H., Nazarian, B., Iding, M., Ringrose, P.S., 2013. Reservoir modeling of CO_2 plume behavior calibrated against monitoring data from Sleipner, Norway. In: SPE Annual Technical Conference and Exhibition. Society of Petroleum Engineers.

Streibel, M., Finley, R.J., Martens, S., Greenberg, S., Möller, F., Liebscher, A., 2014. From pilot to demo scale-comparing Ketzin results with the Illinois Basin-decatur project. Energy Procedia 63, 6323–6334.

Szulczewski, M.L., MacMinn, C.W., Herzog, H.J., Juanes, R., 2012. Lifetime of carbon capture and storage as a climate-change mitigation technology. Proc. Natl. Acad. Sci. U. S. A. 109 (14), 5185–5189.

Yortsos, Y.C., 1995. A theoretical analysis of vertical flow equilibrium. Transp. Porous Media 18 (2), 107–129.

Zheng, Z., Larson, E.D., Li, Z., Liu, G., Williams, R.H., 2010. Near-term mega-scale CO_2 capture and storage demonstration opportunities in China. Energy Environ. Sci. 3 (9), 1153.

Zheng, Z., Soh, B., Huppert, H.E., Stone, H.A., 2013. Fluid drainage from the edge of a porous reservoir. J. Fluid Mech. 718, 558–568.

Zheng, Z., Guo, B., Christov, I.C., Celia, M.A., Stone, H.A., 2015. Flow regimes for fluid injection into a confined porous medium. J. Fluid Mech. 767, 881–909.

Zhou, Q., Birkholzer, J.T., Mehnert, E., Lin, Y.-F., Zhang, K., 2010. Modeling Basin-and plume-scale processes of CO_2 storage for full-scale deployment. Ground Water 48 (4), 494–514.